PHYSICAL REVIEW APPLIED **15,** 034033 (2021)

Controlling the Dynamics of Cloud Cavitation Bubbles through Acoustic Feedback

Kazuki Maeda[1,*] and Adam D. Maxwell[2]

[1] *Center for Turbulence Research, Stanford University, Stanford, California 94305-3024, USA*
[2] *Department of Urology, University of Washington School of Medicine, Seattle, Washington 98195, USA*

(Received 26 November 2020; revised 31 December 2020; accepted 10 February 2021; published 11 March 2021)

Cloud cavitation causes nontrivial energy concentration and acoustic shielding in liquid and its control is a long-standing challenge due to complex dynamics of bubble clouds. We present a framework to study closed-loop control of cavitation through acoustic feedback. While previous approaches have used empirical thresholding, we employ model-based state estimation of coherent bubble dynamics based on theory and high-performance computing. Using a pulsed ultrasound setup, we demonstrate set-point control of the pulse-repetition frequency (PRF) to modulate acoustic cavitation near a solid target over $O(100)$ s. We identify a quasiequilibrium correlation between the PRF and the bubble dynamics and an optimal PRF to minimize acoustic shielding of the target. This framework can be readily scaled up by enhanced acoustic sensing and computational power.

DOI: 10.1103/PhysRevApplied.15.034033

I. INTRODUCTION

The control of cloud cavitation—the nucleation of bubble clusters due to rapid fall of the local pressure in liquid—is a long-standing challenge for optimization of medical and hydraulic systems, as well as sonoluminescence and sonochemistry [1–10]. For example, in extracorporeal ultrasound (US) therapy, the tensile component of high-intensity focused ultrasound (HIFU) can nucleate cavitation bubbles in the human body. These bubbles oscillate violently and collapse on a submicrosecond time scale to cause damage in surrounding materials [8,11–13] as well as acoustic shielding of the targets [14,15]. The intensity of cavitation can largely fluctuate due to the nonequilibrium stochastic nature of nucleation events, depending on the applied pressure fields [16]. Once nucleated, bubble clouds can persist and proliferate by subsequent waves that arrive before dissolution [17–19]. These fascinating bubble dynamics have been quantified through advanced experiments [10,20,21], although direct observation is limited to specialized setups. In practice, far-field bubble-scattered acoustic signals are the only observable quantities. For US-induced acoustic cavitation, open-loop control of the US waveform has been explored to favorably trigger violent collapse of bubble clouds to enhance cavitation erosion [22]. Closed-loop control has been utilized to excite stationary cavitation by modulating incident US waves, such that stable acoustic feedback is maintained [23–28]. These systems, however, rely on empirical thresholds and lack a quantifiable state estimation of cavitation, as the bubble dynamics are not modeled in the feedback loop. This limitation motivates us to pursue model-based feedback control, not only to stabilize cavitation but also to modulate cavitation based on a quantitative state estimation.

The modeling of cloud cavitation has been extensively explored in past decades [29]. A recent effort has identified a scaling parameter that dictates the coherent dynamics of spherical bubble clouds in ultrasound fields, *the dynamic cloud-interaction parameter*: $B_D = N < R_b > /R_c$, where N and R_b are the total number and the average radius of bubbles in the cloud, R_c is the radius of the cloud, and $<>$ denotes the time average during periodic oscillations [30]. The parameter characterizes the structure of bubble clouds and the bubble-induced acoustic fields. In the limit of linear oscillations of bubbles, a static form of such a parameter can be obtained using mean-field theory [31]. B_D has been derived from first-principles hydrodynamic many-body theory and extends to nonlinear dynamics of cavitation bubbles that grow far from equilibrium. In experiments, correlations have been identified between the energy state of bubble clouds and the bubble-scattered acoustic waves [15,30]. These results are promising for real-time estimation of bubble dynamics through acoustic measurements [32]. In this work, we design a framework to study model-based closed-loop control of cloud cavitation through acoustic feedback and demonstrate its implementation in a pulsed US system.

---

[*] kemaeda@stanford.edu

II. METHODS

A. Theory and setup

Figure 6 shows the schematic of the control and the US setup. In the setup, pulses of a US wave are generated by a transducer and focused on a cylindrical target made of epoxy resin, with a base diameter and length of 6.25 and 10 mm, respectively, in water. Each pulse contains ten cycles of a sinusoidal wave packet with a frequency of 340 kHz and a peak focal amplitude of 7.0 MPa. Following our previous study, the water is degassed to realize an O_2 level of 65% saturation [15]. The O_2 level is positively correlated with the intensity of cavitation since the concentration of noncondensible gas in water controls the number of nuclei that are cavitated, as well as the violence of the cavitation collapse and the postcollapse bubble-dissolution rate. Although the present setup is focused on the specific state of water for demonstration, the control framework is in principle not limited by the concentration of noncondensible gas. During the passage of the wave, a layer of cavitation bubbles is nucleated on the proximal surface of the target to cause energy shielding. The acoustic waves scattered by the bubbles are measured using an array transducer. Further technical details of this setup (without control) are described elsewhere [15]. The controller varies the pulse-repetition frequency (PRF); the intensities of both cavitation and the bubble-scattered acoustics are positively correlated with the PRF [Figs. 6(b) and 6(c)]; a high PRF indicates a short pulse interval. With a short interval, fewer bubbles dissolve before the next pulse arrives. The pulse causes growth and violent collapse of the bubbles, leading to proliferation of daughter bubbles that serve as nuclei in the subsequent pulse (see Appendix A). For the dense cloud [Fig. 6(c)], the bubbles in the cloud most proximal to the transducer experience greater acoustic pressure due to shielding and are excited more than the distal ones. A similar anisotropic structure has previously been observed in isolated spherical bubble clouds [30]. The measurement is used to estimate the energy that is transmitted across the bubble clouds into the target. Based on the offset of the estimation from a set point, a proportional-integral (PI) controller varies the PRF, but with a constant pressure amplitude, to modulate cavitation and to achieve the set-point value. Various types of controller can be used instead. Using the setup, we experimentally demonstrate real-time control of cavitation during $O(100)$ s of pulsed US radiation and identify an empirical correlation between the PRF and the bubble dynamics, and an optimal PRF to minimize the shielding by cavitation.

The acoustic signals measured at each array element are projected onto a correlation-based imaging functional F [33], which is used as an estimator input. F is a normalized measure of the amplitude of the coherent acoustic scattering from the target region: $F = I/I_0$, where

$$I = \max_{\mathbf{z}}\left[\sum_{j,l} C_T[\tau(\mathbf{z},\mathbf{x}_j)+\tau(\mathbf{z},\mathbf{x}_l),\mathbf{x}_j,\mathbf{x}_l]\right], \tag{1}$$

and C_T is the cross-correlation of the signals:

$$C_T(\tau,\mathbf{x}_j,\mathbf{x}_l) = \frac{1}{T}\int_0^T u(t,\mathbf{x}_j)u(t+\tau,\mathbf{x}_l)dt, \tag{2}$$

where $u(t,\mathbf{x}_j)$ is the signal at the jth array at $\mathbf{x}_j$ at time t, $\mathbf{z}$ is the coordinate of the domain, and T is the time horizon of the process. $\tau(\mathbf{z},\mathbf{x})$ is the acoustic travel time from $\mathbf{z}$ to $\mathbf{x}$. I_0 is the reference value obtained in a case without bubbles.

The estimator outputs a scalar variable E, which is defined as the energy transmitted across the bubbles into the target, normalized by the reference value obtained without bubbles. This choice of the input and output parameters is based on a first-principles model for the dynamics of bubble clouds. The kinetic energy of incompressible potential flow induced by oscillations of interacting spherical bubbles can be expressed as

$$K = 2\pi\rho_l\sum_{i=1}^{N}\left[R_i^3\dot{R}_i^2 + \sum_{j\neq i}^{N}\frac{R_i^2R_j^2\dot{R}_i\dot{R}_j}{r_{ij}}\right] + (H.O.T.), \tag{3}$$

where R_i, $\dot{R}_i$, and r_{ij} are the radius and the radial velocity of bubble i, and the distance between the centers of bubbles i and j, respectively. For a cloud with $N \gg 1$, the kinetic energy can be approximated as

$$K \approx 2\pi\rho_l N < R^3\dot{R}^2 > (1+B_d), \tag{4}$$

where $B_d = N < R > /L$. L is the length scale of the inter-bubble interaction. B_d is therefore a measure of the relative contribution of the coherence among bubbles. Hydrodynamically, B_d corresponds to the scale of the added inertia of a bubble cloud. For a spherical bubble cloud, $L \sim R_c$ and B_d corresponds to the aforementioned dynamic interaction parameter. For the present bubbly layer, $L \sim R_t$, where R_t is the radius of the base of the target. Since the bubble cloud is the only component that dynamically alters the energy state of the system, both E and F are expected to be scaled by $B_d : B_d = N < R > /R_t$ and thus these variables are correlated, regardless of N and $< R >$.

B. Simulation-based estimator

Based on this physical insight, we conduct numerical experiments to obtain the quantitative correlation between E and F. A coupled Eulerian-Lagrangian method is employed for the simulation [34]. In the method, we formulate the dynamics of the multicomponent mixture using the compressible multicomponent Navier-Stokes equation. We model the cylindrical target as an elastic solid with zero shear modulus, with a density of 1200 kg m^{-3} and a longitudinal sound speed of 2440 m s^{-1}. The coupled dynamics of the target and the surrounding water are modeled using an interface-capturing method [35,36]. For modeling the dynamics of the bubble cloud excited in an ultrasound field, we use an Eulerian-Lagrangian method. The method has been derived previously and validated in detail [37] and applied to parametric simulation of the dynamics of spherical bubble clouds excited by burst waves [15]. We provide a brief summary of the method here. In the method, we describe the dynamics of a bubbly mixture using volume-averaged equations of motion [38–41]:

$$\frac{\partial \overline{\rho}}{\partial t} + \nabla \cdot (\overline{\rho \mathbf{u}}) = 0, \tag{5}$$

$$\frac{\partial (\overline{\rho \mathbf{u}})}{\partial t} + \nabla \cdot (\overline{\rho \mathbf{u}} \otimes \overline{\mathbf{u}} + p\mathcal{I} - \mathcal{T}) = 0, \tag{6}$$

$$\frac{\partial \overline{E}}{\partial t} + \nabla \cdot \left((\overline{E} + p)\overline{\mathbf{u}} - \mathcal{T} \cdot \overline{\mathbf{u}} \right) = 0, \tag{7}$$

where ρ is the density, $\mathbf{u} = (u, v, w)^T$ is the velocity, $\underline{p}$ is the pressure and E is the total energy, respectively. $\overline{(\cdot)}$ denotes the volume-averaging operator that acts on arbitrary field variables $(\cdot)$: $\overline{(\cdot)} = (1 - \beta)(\cdot)_l + \beta(\cdot)_g$, where $\beta \in [0, 1)$ is the volume fraction of gas (the void fraction) and subscripts l and g denote the liquid and gas phase, respectively. $\mathcal{T}$ is the effective viscous stress tensor of the mixture, which we approximate as that of the liquid phase: $\mathcal{T} \approx \mathcal{T}_l$. We invoke two approximations that are valid at the limit of low void fraction: the density of the mixture is approximated by that of the liquid—$\overline{\rho} \approx (1 - \beta)\rho_l$; and the slip velocity between the two phases is zero—$\overline{\mathbf{u}} \approx \mathbf{u}_l = \mathbf{u}_g$.

Equations (5)–(7) can then be rewritten as conservation equations in terms of the mass, momentum, and energy of the liquid with source terms, as an inhomogeneous hyperbolic system:

$$\frac{\partial \mathbf{q}_l}{\partial t} + \nabla \cdot \mathbf{f}(\mathbf{q}_l) = \mathbf{g}(\mathbf{q}_l, \beta, \dot{\beta}), \tag{8}$$

where

$$\mathbf{q}_l = [\rho_l, \rho_l \mathbf{u}_l, E_l]^T, \tag{9}$$

$$\mathbf{f} = [\rho_l \mathbf{u}_l, \rho_l \mathbf{u}_l \otimes \mathbf{u}_l + p\mathcal{I} - \mathcal{T}_l, (E_l + p)\mathbf{u}_l - \mathcal{T}_l \cdot \mathbf{u}_l]^T, \tag{10}$$

and

$$\mathbf{g} = \frac{1}{1 - \beta}\frac{d\beta}{dt}\mathbf{q}_l - \frac{\beta}{1 - \beta}\nabla \cdot (\mathbf{f} - \mathbf{u}_l \mathbf{q}_l). \tag{11}$$

For a thermodynamic closure for the liquid, we employ the stiffened gas equation of state:

$$p = (\gamma - 1)\rho\varepsilon - \gamma\pi_\infty, \tag{12}$$

where ε is the internal energy of the liquid, γ is the specific heat ratio, and π_∞ is the stiffness, respectively. In the present study, we use $\gamma = 7.1$ and $\pi_\infty = 3.06 \times 10^8$ Pa for water.

To model the gas phase, we employ a Lagrangian point-bubble approach, in that the gas is treated as spherical radially oscillating cavities consisting of a noncondensible air and liquid vapor. In the simulation, we assume that a finite number of bubbles are initially distributed near the focal target. This condition models the experimental setup in that preexisting nuclei of noncondensible gas are mixed with vapor, many of which are excited in the previous pulse and remain until the subsequent pulses arrive. Note that in clean pure liquid, vapor bubbles can grow without such preexisting nuclei (homogeneous nucleation). In these ideal conditions, the nucleation can be directly modeled [42–45]. The center of the nth bubble ($n \in \mathbb{Z} : n \in [1, N]$), with a radius of R_n and a radial velocity of $\dot{R}_n$, is initially defined at the coordinate $\mathbf{x}_n$ and tracked as Lagrangian points during the simulations. To define the continuous field of the void fraction in the mixture at coordinate $\mathbf{x}$, we smear the volume of bubble using a regularization kernel δ:

$$\beta(\mathbf{x}) = \sum_{n=1}^{N} V_n(R_n)\delta(d_n), \tag{13}$$

where V_n is the volume of bubble n, $V_n = 4\pi/3R_n^3$, and d_n is the distance of the coordinate $\mathbf{x}$ from the center of the bubble, $d_n = |\mathbf{x} - \mathbf{x}_n|$. Throughout the present study, we use a second-order Gaussian function for δ with a kernel width of 1.1Δ, where Δ is the grid width. For numerical representation, we discretize Eq. (8) on an axisymmetric grid and spatially integrate using a fifth-order finite-volume weighted essentially nonoscillatory (WENO) scheme [36]. A fourth- or fifth-order Runge-Kutta-Cash-Karp (RKCK) algorithm [46] is employed for time integration of solutions.

To model the dynamics of volumetric oscillations of bubbles, we employ the Keller-Miksis equation [47]:

$$\left[R_n\left(1 - \frac{\dot{R}_n}{c}\right)\right]\ddot{R}_n + \frac{3}{2}\dot{R}^2\left(1 - \frac{\dot{R}_n}{3c}\right) = \frac{p_n - p_\infty}{\rho}\left(1 + \frac{\dot{R}_n}{c}\right) + \frac{R_n \dot{p}_n}{\rho c}, \tag{14}$$

where p_n is the pressure at the bubble wall:

$$p_n = p_{Bn} - \frac{4\mu_l \dot{R}_n}{R_n} - \frac{2\sigma}{R_n}. \tag{15}$$

p_{Bn} is the pressure inside the bubble, σ is the surface tension, and p_∞ is the component of the pressure that forces the radial oscillations of the bubble. We use a reduced-order model to account for heat and mass transfer across the bubble-liquid interface [48].

The grid size is uniform, with a radial and axial width of $\Delta = 100$ μm in the target-wave interaction region. We track the radial evolution of the bubbles at the subgrid scale and resolve the bubble-scattered acoustics on the grid. The parameters are chosen as discussed below.

This numerical setup is designed to fully mimic the physical setup. In the initial condition, Lagrangian bubble nuclei with a uniform radius of 10 μm are randomly distributed in the cylindrical region on the proximal base of the target. A previous study has identified that the dynamics of cavitation bubble clouds are insensitive to the polydispersity of the nuclei, when excited by ultrasound waves in regimes similar to those considered in the present study [30]. Oscillations of the bubbles are tracked as solutions of the Keller-Miksis equation. The US wave and bubble-scattered pressure waves are computed as solutions of the compressible Navier-Stokes equations on a structured Eulerian grid with a sufficiently high resolution (for further details of the method, see Appendix A). Twenty cases are simulated during the passage and scattering of a single US pulse, with various values of the number density of the bubble, n, and the thickness of the bubbly layer, h, within the ranges of $0 \leq h \leq 1.0$ mm and $0 \leq n \leq 9.6$ mm^{-3}, respectively. Figures 2(a) and 2(c) show snapshots of the bubbles during the passage of the US with $(n, h) = (1.2, 0.25)$ and $(9.6, 1.0)$, at the same instance as in the experimental images [Figs. 6(b) and 6(c)]. Figures 3(b) and 3(d) show the contours of the maximum pressure on the cross-plane throughout the same simulations, $p_{\max}$, respectively. The morphology of the numerical bubble clouds is similar to that in the experimental images. The anisotropic structure is clear in the dense numerical cloud. In the pressure contours, the region with a high maximum pressure ($p_{\max} > 6$ MPa) is widely distributed in the proximal interior of the target with the dilute bubbles, while the maximum pressure is nominally small ($p_{\max} < 4$ MPa) in the target with the dense cloud. These results indicate that the US wave penetrates into the target across the small bubble cloud, while a large portion of the wave

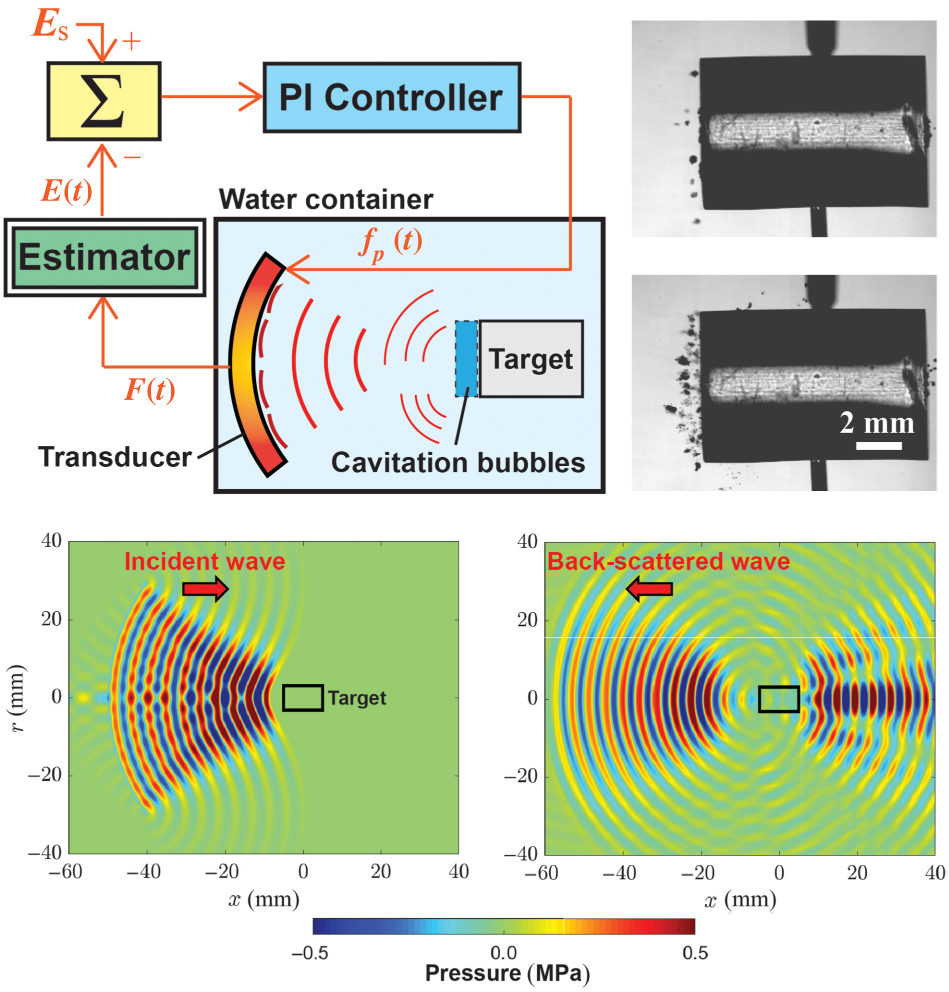

FIG. 1. (a) A schematic of the setup. A transducer generates US pulses focused on a cylindrical target, aligned on the acoustic axis, and measures the back-scattered acoustic waves, in a water container. A model-based feedback controller modulates the PRF, denoted as $f_p(t)$, based on the estimation of the energy transmitted into the target, E. (b),(c) Experimental high-speed images of bubble clouds with a PRF of (b) 10 Hz and (c) 100 Hz during a short-term exposure of US pulses. (d),(e) The instantaneous pressure contour during the propagation of (d) the incident US wave obtained from a representative numerical simulation and (e) the wave scattered by the target shielded by a bubbly layer.

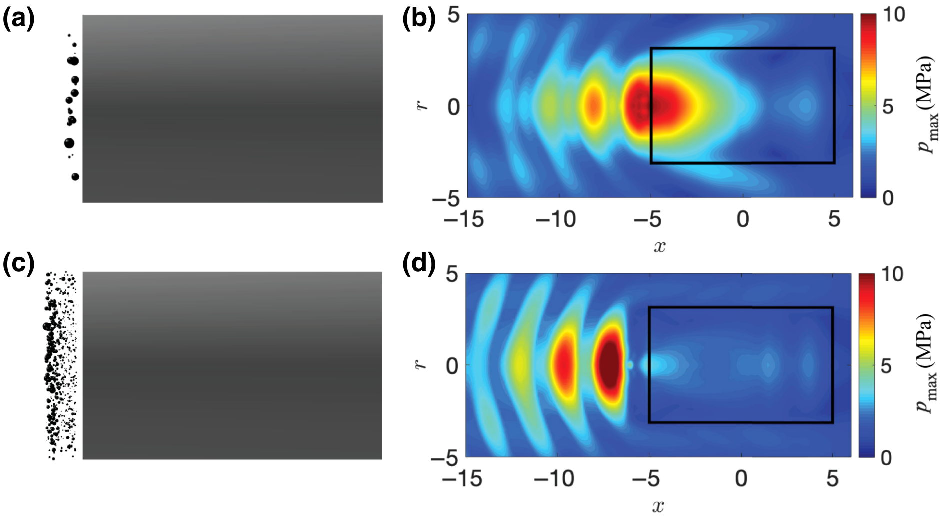

FIG. 2. (a),(c) Side views of the bubbly layers and the target obtained from the simulations that model the low- and high-PRF cases during the passage of the US wave, with $(n, h) = (1.2, 0.25)$ and $(9.6, 1.0)$. An anisotropic structure, in that the proximal bubbles are more excited than the distal bubbles, is evident in the latter image. (b),(d) Distributions of the maximum pressure during the course of the same simulations.

energy is scattered by the large cloud. In the latter contour, clear vertical bands of high pressure are observed in the proximal liquid, which can be explained by the interference of the reflected and incoming parts of the wave.

To quantify the anisotropy, we use the normalized moment of kinetic energy, μ_K, defined as

$$\mu_K = \frac{\sum_{i=1}^{N} K_i(x_i - x_c)}{\sum_{i=1}^{N} K_i h}, \tag{16}$$

where K_i is the kinetic energy of incompressible liquid induced by the oscillations of the ith bubble, $K_i = 2\pi\rho R_i^3 \dot{R}^2$, where x_i is the coordinate of bubble i along the acoustic axis, and x_c is the center of the cloud: $x_c = \sum_{i=1}^{N} x_i/N$. A negative μ_k indicates the spatial bias of active bubbles in the proximal side of the cloud. A similar moment has previously been used to characterize the energy state of spherical bubble clouds [30].Figures 3(a)–3(c), respectively, show correlations of μ_K, E, and F against B_d, obtained from the simulation. The data points are collapsed well along a single curve, indicating invariance to the number of bubbles. μ_K and

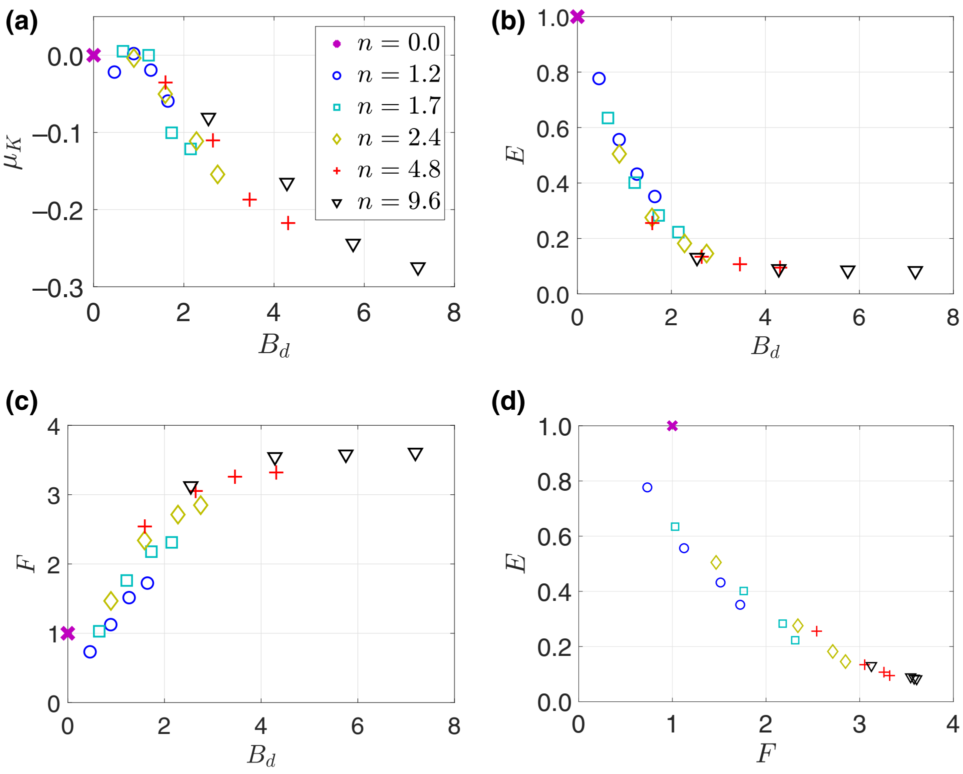

FIG. 3. (a)–(c) Correlations of μ_k, E, and F against B_d, respectively. The number density of the bubble, n mm^{-3}, and the thickness of the bubble cloud, h ($0 < h < 1.0$ mm), are varied. (d) The correlation of E and F. The fitting function serves as the state estimator shown in Fig. 6(a).

E decrease, while F increases with increasing B_d. E and F become invariant for $B_d > 4$, indicating that the energy shielding is saturated in this regime. Figure 3(d) shows correlations between E and F. The data points are well collapsed on a single curve. Note that the E–F correlation is not guaranteed to be linear due to the nonlinear dynamics of bubbles. The numerical simulation is therefore critical to obtain this correlation. Note also that the correlation is nonmonotonic for $F < 1$; the reference state without bubbles ($n = 0$) is placed at $(F, E) = (1, 1)$. This anomaly can be explained by the breakdown of the scaling with B_d, for small N.

These analyses indicate that the bubble dynamics are dictated by the interaction parameter and the acoustic wave and the energy transmission are monotonically correlated, as predicted by the theory. With the increase in this parameter, the anisotropy and the scattering are enhanced, while the energy transmission is decreased. From a macroscopic point of view, the greatest portion of the acoustic energy is scattered by only the surface bubbles when clouds are thick and/or dense, while otherwise a large portion of the acoustic energy is transmitted and all bubbles oscillate in a similar manner regardless of their locations. We apply nonlinear regression to the data in Fig. 3(d) to obtain a fitting function. This function serves as the estimator that uniquely outputs E against a real-time input of F, for $F > 1$. Due to the data-driven nature of the estimator, we do not expect that the estimation is accurate for bubble clouds the state of which is far from that considered in the simulation database. Conversely, for accurate estimation, it is desirable to have prior knowledge about the expected state of cavitation when constructing the database; for instance, through preliminary experiments.

III. CONTROL DEMONSTRATION

Figures 4(a)–4(c), respectively, show the evolution of the energy transmission outputted by the estimator, that of the imaging functional, and that of the PRF outputted by the controller during US radiation, with four distinct values of the set point: $E_s = [0.2, 0.3, 0.4, 0.5]$. The feedback rate is $f_P/5$ Hz, where f_P is the PRF, and $K_P = 20$ and $K_I = 20$ are used for the proportional and integral gains of the controller. At around $t = 100$ s, both E and F reach their steady states and then oscillate around constant values. The values of E at the steady states correspond to the set-point values, for all cases. Similarly, the PRF evolves with constant oscillations around its stationary values for $t > 100$ s, in the range of $20 < f_P < 70$ Hz. Note that without control, cavitation bubbles intermittently proliferate over the time scale considered in the present study and this phenomenon is not even reproducible trial by trial. Such proliferating cavitation is not included in the numerical database and is therefore outside of the range of the present estimator [Fig. 3(d)]. Although it is known that the increase in PRF can enhance the intensity of acoustic cavitation [17–19,49], there exists no quantitative measure to uniquely specify the bubble dynamics given the PRF, due to this high nonstationarity. With the real-time control, cavitation can achieve quasiequilibrium over pulses. We are thus motivated to correlate the PRF (the controller output) and the transmitted energy (the estimator output) in these states. Figure 5(a) shows the correlation. For $f_P < 5$ Hz, we do not observe bubbles and $F < 1$. In this range, we set E to unity. For $f_P > 5$ Hz, the energy decreases monotonically, indicating the enhancement of cavitation with increasing f_P. In order to further characterize the correlation between the PRF and the energy transmission, we define the effective rate of energy delivery to the target excluding the portion scattered by the bubbly layer, the *effective PRF*: $f_{EP} = Ef_P$. Interestingly, f_{EP} has a convex profile and takes a peak value of 14.6 Hz at $f_{PC} = 35$ Hz [Fig. 4(b)], which can be interpreted as the optimal PRF for energy transmission. For $f_P < 5$ Hz, $E = 1$, and $f_P = f_{EP}$, there is no cavitation effect. For $f_P < 5$ Hz,

$$\frac{\partial f_{EP}}{\partial f_P} = E + f_P \frac{\partial E}{\partial f_P} \approx E + \gamma f_P, \tag{17}$$

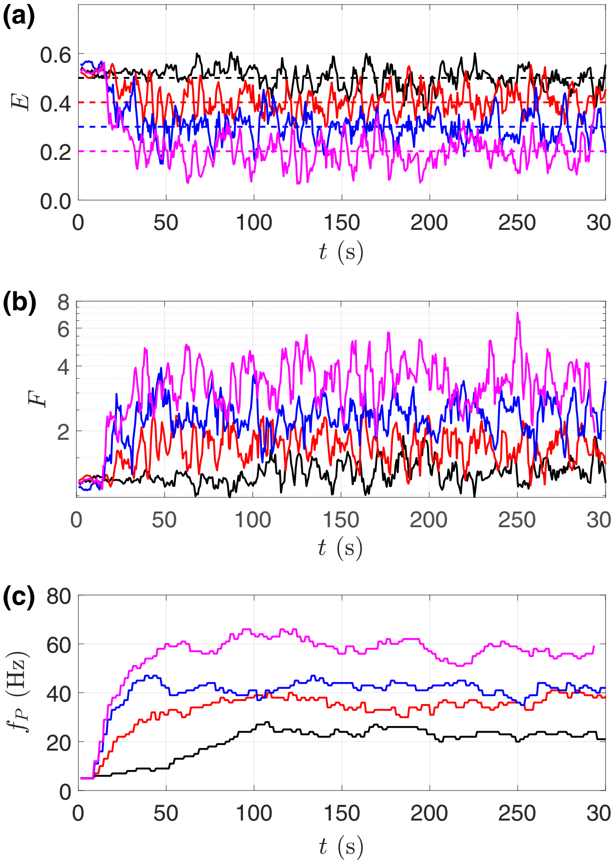

FIG. 4. The evolution of (a) E, (b) F, and (c) the PRF during feedback control with set-point values of $E_s = [0.2, 0.3, 0.4, 0.5]$. The dotted lines in (a) denote set-point values.

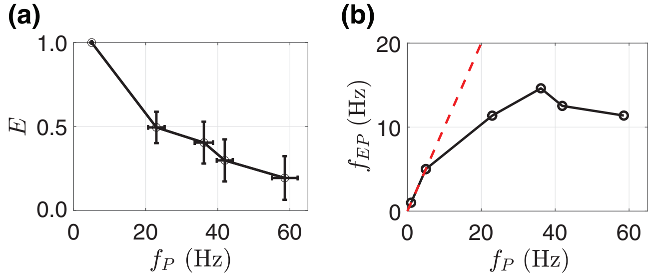

FIG. 5. (a)The energy transmitted into the target, E, as a function of the actual PRF. Both variables are averaged over the period of the feedback control during $100 < t < 300$ s. (b) The effective PRF as a function of the actual PRF, in terms of the mean values during feedback control. The dotted line denotes the linear reference with $E = 1$.

where γ is a constant that approximates the slope of E: $\partial E/\partial f_P \approx \gamma < 0$. $\partial^2 f_{EP}/\partial f_P^2 \approx 2\gamma < 0$, indicating the convexity of f_{EP}. For $5 < f_P < f_{PC}$, both E and γf_P decrease with increasing f_P, while it remains that $\partial f_{EP}/\partial f_P > 0$; the rate of increase in f_P is more dominant than that of the energy loss due to cavitation, represented by E and γf_P, respectively, on the right-hand side of Eq. (17). Then, at $f_P \approx f_{PC}$, $\partial f_{EP}/\partial f_P = 0$ and f_P reaches the maximum value. For $f_P > f_{PC}$, $\partial f_{EP}/\partial f_P < 0$; f_{EP} decreases with f_P since γf_P is dominant. At even higher f_P, $E < 0.2$; the cavitation and energy shielding become further enhanced. In this regime, the present estimator tends to become inaccurate; the state of the bubble cannot be uniquely identified by E, as seen in the saturation of E against B_d.

IV. CONCLUSION

In conclusion, we design a framework for model-based closed-loop control of cavitation through acoustic feedback, by using a data-driven state estimator. In our demonstration using a US system, set-point control of PRF-modulated cloud cavitation near a solid target is designated and we identify an optimal PRF that can minimize the cavitation-induced energy shielding. Although the nucleation and dissolution of bubbles are not explicitly modeled, the control system can implicitly maintain and quantify the balance between those phenomena in dynamic equilibrium, through the correlation of estimation and control. This system is a demonstration of optimization of cavitation by means of controlling the PRF. The system can be particularly useful for optimizing energy transfer to a target in HIFU-based medical therapies. For different applications, the control framework can permit other sets of estimation and control parameters. For example, one can consider estimating the maximum pressure due to bubble-cloud collapse and control of the US amplitude, to modulate the cavitation damage of a target. The accuracy of the state estimation and control depends on the quality of the numerical data and the acoustic measurements. Therefore, the framework can be scaled up with enhanced computational power and precision acoustic sensing.

ACKNOWLEDGMENTS

K.M. acknowledges the National Institutes of Health (NIH) under Grant No. P01-DK043881 and the Extreme Science and Engineering Discovery Environment (XSEDE), which is supported by the National Science Foundation (NSF) under Grant No. TG-CTS190009. A.D.M. acknowledges the NIH under Grants No. P01-DK043881 and No. K01-DK104854.

APPENDIX A: RESPONSE OF CAVITATION TO A STEP CHANGE IN THE PULSE-REPETITION FREQUENCY

In this appendix, we present data on the response of cavitation to the PRF during a short-time exposure in our setup. Without control, we send 480 pulses with the same waveform, following that used in the main text, but a time-varying PRF: $f_P = 200$ Hz from the first through the 160th pulse; $f_P = 10$ Hz from the 181th through the 320th pulse; and $f_P = 200$ Hz thereafter. During the passage of each pulse, we capture a high-speed image of the cavitation bubbles and concurrently use the estimator to obtain the energy transmission E. The high-speed camera is triggered 35 μs after the head of each pulse arrives at the target, at which the bubble cloud is expected to reach its maximum volume during the passage of the pulse. This trigger timing is consistent with both experimental and numerical images presented in this study [Figs. 6(b) and 6(c), Fig. 2, and Fig. 6(a)]. In the images, we compute the total area occupied by bubbles within the rectangular region on the proximal surface of the target [solid line in Fig. 6(a)], A mm^2.Figure 6 shows the results. Both A and E show distinct forms of behavior against the two values of PRF. When $f_P = 200$ Hz, the area and the imaging functional largely oscillate around $A \approx 0.5$ and $E \approx 0.4$, respectively. When $f_P = 10$ Hz, they oscillate with smaller amplitudes around $A \approx 0.1$ and $E \approx 0.6$, respectively. As mentioned in the main text, at this high PRF without control, the bubbles grow not only near the target but also far from the target [e.g., bubbles outside the rectangular region in Fig. 6(a)]. The observation of such outlying bubbles is not statistically repeatable and is not modeled in the numerical experiment. The estimator is not designed to capture their effect and the large-amplitude oscillations of E here may not provide quantitative information. Nevertheless, the instant changes of both A and E following the step changes of the PRF indicates the strong positive dependency of the intensity of cavitation on the PRF.

Note again that, during a longer time scale of exposure without control in our setup, the response of the bubbles

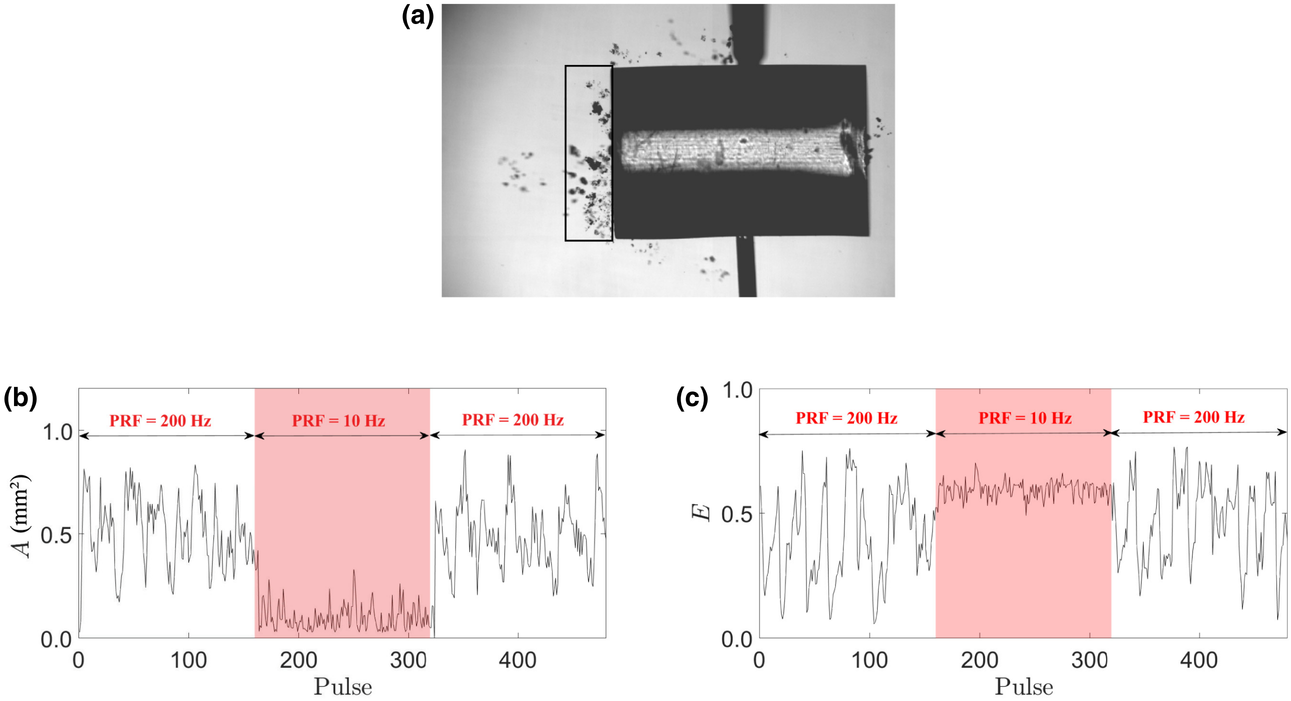

FIG. 6. (a) A representative image of the cavitation bubbles during the passage of a US pulse with $f_P = 200$ Hz without control. (b) The evolution of the area of bubbles in the rectangular region in Fig. 6(a). (c) The corresponding evolution of the transmitted energy outputted by the estimator.

can become nonstationary and nonrepeatable, due likely to the intermittent growth and proliferation of the outlying bubbles far from the target.

[1] M. Plesset and A. Ellis, On the mechanism of cavitation damage, Trans. ASME **77**, 1055 (1955).
[2] M. Plesset and A. Prosperetti, Bubble dynamics and cavitation, Annu. Rev. Fluid Mech. **9**, 145 (1977).
[3] L. Crum, Tensile strength of water, Nature **278**, 148 (1979).
[4] K. A. Mørch, in *Cavitation and Inhomogeneities in Underwater Acoustics* (Springer, Berlin, Heidelberg, 1980), p. 95.
[5] G. Reisman, Y.-C. Wang, and C. Brennen, Observations of shock waves in cloud cavitation, J. Fluid Mech. **355**, 255 (1998).
[6] K. Suslick, Y. Didenko, M. Fang, T. Hyeon, K. Kolbeck, W. McNamara III, M. Mdleleni, and M. Wong, Acoustic cavitation and its chemical consequences, Philos. Trans. R. Soc. London, A: Math. Phys. Eng. Sci. **357**, 335 (1999).
[7] M. Brenner, S. Hilgenfeldt, and D. Lohse, Single-bubble sonoluminescence, Rev. Mod. Phys. **74**, 425 (2002).
[8] Y. Pishchalnikov, O. Sapozhnikov, M. Bailey, J. Williams Jr, R. Cleveland, T. Colonius, L. Crum, A. Evan, and J. McAteer, Cavitation bubble cluster activity in the breakage of kidney stones by lithotripter shockwaves, J. Endourol. **17**, 435 (2003).
[9] K. Ando, A.-Q. Liu, and C.-D. Ohl, Homogeneous Nucleation in Water in Microfluidic Channels, Phys. Rev. Lett. **109**, 044501 (2012).
[10] C. Cairós and R. Mettin, Simultaneous High-Speed Recording of Sonoluminescence and Bubble Dynamics in Multibubble Fields, Phys. Rev. Lett. **118**, 064301 (2017).
[11] L. Crum, Cavitation microjets as a contributory mechanism for renal calculi disintegration in ESWL, J. Urol. **140**, 1587 (1988).
[12] C. Coussios, C. Farny, G. Ter Haar, and R. Roy, Role of acoustic cavitation in the delivery and monitoring of cancer treatment by high-intensity focused ultrasound (HIFU), Int. J. Hyperthermia **23**, 105 (2007).
[13] P. Movahed, W. Kreider, A. Maxwell, S. Hutchens, and J. Freund, Cavitation-induced damage of soft materials by focused ultrasound bursts: A fracture-based bubble dynamics model, J. Acoust. Soc. Am. **140**, 1374 (2016).
[14] Y. A. Pishchalnikov, J. A. McAteer, M. R. Bailey, I. V. Pishchalnikova, J. C. Williams Jr, and A. P. Evan, in *AIP Conf. Proc.*, Vol. 838 (American Institute of Physics, PA, USA, 2006), p. 319.
[15] K. Maeda, A. Maxwell, T. Colonius, W. Kreider, and M. Bailey, Energy shielding by cavitation bubble clouds in burst wave lithotripsy, J. Acoust. Soc. Am. **144**, 2952 (2018).
[16] A. Brotchie, F. Grieser, and M. Ashokkumar, Effect of Power and Frequency on Bubble-Size Distributions in Acoustic Cavitation, Phys. Rev. Lett. **102**, 084302 (2009).
[17] Y. Pishchalnikov, J. Williams, Jr., and J. McAteer, Bubble proliferation in the cavitation field of a shock wave lithotripter, J. Acoust. Soc. Am. **130**, EL87 (2011).
[18] A. Maxwell, T.-Y. Wang, C. Cain, J. Fowlkes, O. Sapozhnikov, M. Bailey, and Z. Xu, Cavitation clouds created by

shock scattering from bubbles during histotripsy, J. Acoust. Soc. Am. **130**, 1888 (2011).

[19] S. Frank, J. Lautz, G. Sankin, A. Szeri, and P. Zhong, Bubble Proliferation or Dissolution of Cavitation Nuclei in the Beam Path of a Shock-Wave Lithotripter, Phys. Rev. Appl. **3**, 034002 (2015).

[20] N. Bremond, M. Arora, C. Ohl, and D. Lohse, Controlled Multibubble Surface Cavitation, Phys. Rev. Lett. **96**, 224501 (2006).

[21] S.-W. Ohl, E. Klaseboer, and B. Khoo, Bubbles with shock waves and ultrasound: A review, Interface Focus **5**, 20150019 (2015).

[22] T. Ikeda, S. Yoshizawa, M. Tosaki, J. Allen, S. Takagi, N. Ohta, T. Kitamura, and Y. Matsumoto, Cloud cavitation control for lithotripsy using high intensity focused ultrasound, Ultrasound Med. Biol. **32**, 1383 (2006).

[23] C. Thomas, C. Farny, C. Coussios, R. Roy, and R. Holt, Dynamics and control of cavitation during high-intensity focused ultrasound application, Acoust. Res. Lett. Online **6**, 182 (2005).

[24] N. Hockham, C. Coussios, and M. Arora, A real-time controller for sustaining thermally relevant acoustic cavitation during ultrasound therapy, IEEE Trans. Ultrason. Ferroelectr. Freq. Control **57**, 2685 (2010).

[25] A. Sabraoui, C. Inserra, B. Gilles, J.-C. Béra, and J.-L. Mestas, Feedback loop process to control acoustic cavitation, Ultrason. Sonochem. **18**, 589 (2011).

[26] K. Saalbach, H. Ohrdes, and J. Twiefel, Closed loop cavitation control—a step towards sonomechatronics, Ultrason. Sonochem. **44**, 14 (2018).

[27] A. Patel, S. Schoen, and C. Arvanitis, Closed-loop spatial and temporal control of cavitation activity with passive acoustic mapping, IEEE Trans. Bio-Med. Eng. **66**, 2022 (2018).

[28] C. Tan, Y. Li, T. Han, C. Alfred, and P. Qin, in *2019 IEEE International Ultrasonics Symposium (IUS)* (IEEE, Glasgow, United Kingdom, 2019), p. 2295.

[29] C. E. Brennen, *Cavitation and Bubble Dynamics* (Cambridge University Press, 2014), https://www.google.com/books/edition/Cavitation_and_Bubble_Dynamics/hX8PAQAAQBAJ?hl=en&gbpv=0.

[30] K. Maeda and T. Colonius, Bubble cloud dynamics in an ultrasound field, J. Fluid Mech. **862**, 1105 (2019).

[31] L. d'Agostino and C. Brennen, Linearized dynamics of spherical bubble clouds, J. Fluid Mech. **199**, 155 (1989).

[32] K. Maeda, Ph.D. thesis, California Institute of Technology, 2018.

[33] J. Garnier and G. Papanicolaou, Passive sensor imaging using cross correlations of noisy signals in a scattering medium, SIAM J. Imaging Sci. **2**, 396 (2009).

[34] K. Maeda and T. Colonius, Eulerian-Lagrangian method for simulation of cloud cavitation, J. Comput. Phys. **371**, 994 (2018).

[35] G. Perigaud and R. Saurel, A compressible flow model with capillary effects, J. Comput. Phys. **209**, 139 (2005).

[36] V. Coralic and T. Colonius, Finite-volume WENO scheme for viscous compressible multicomponent flows, J. Comput. Phys. **274**, 95 (2014).

[37] K. Maeda and T. Colonius, A source term approach for generation of one-way acoustic waves in the Euler and Navier-Stokes equations, Wave Motion **75**, 36 (2017).

[38] A. Biesheuvel and L. vanWijngaarden, Two-phase flow equations for a dilute dispersion of gas bubbles in liquid, Annu. Rev. Fluid Mech. **148**, 301 (1984).

[39] K. Commander and A. Prosperetti, Linear pressure waves in bubbly liquids: Comparison between theory and experiments, J. Acoust. Soc. Am. **85**, 732 (1989).

[40] M. Kameda and Y. Matsumoto, Shock waves in a liquid containing small gas bubbles, Phys. Fluids **8**, 322 (1996).

[41] D. Fuster and T. Colonius, Modeling bubble clusters in compressible liquids, J. Fluid Mech. **688**, 352 (2011).

[42] M. Blander and J. Katz, Bubble nucleation in liquids, AIChE J. **21**, 833 (1975).

[43] V. K. Shen and P. G. Debenedetti, Density-functional study of homogeneous bubble nucleation in the stretched Lennard-Jones fluid, J. Chem. Phys. **114**, 4149 (2001).

[44] J. Diemand, R. Angélil, K. Tanaka, and H. Tanaka, Large scale molecular dynamics simulations of homogeneous nucleation, J. Chem. Phys. **139**, 074309 (2013).

[45] M. Gallo, F. Magaletti, D. Cocco, and C. Casciola, Nucleation and growth dynamics of vapour bubbles, J. Fluid Mech. **883**, A14 (2020).

[46] J. Cash and A. Karp, A variable order Runge-Kutta method for initial value problems with rapidly varying right-hand sides, ACM Trans. Math. Software **16**, 201 (1990).

[47] J. Keller and M. Miksis, Bubble oscillations of large amplitude, J. Acoust. Soc. Am. **68**, 628 (1980).

[48] A. Preston, T. Colonius, and C. Brennen, A reduced-order model of diffusive effects on the dynamics of bubbles, Phys. Fluids **19**, 123302 (2007).

[49] T. Horiba, T. Ogasawara, and H. Takahira, Cavitation inception pressure and bubble cloud formation due to the backscattering of high-intensity focused ultrasound from a laser-induced bubble, J. Acoust. Soc. Am. **147**, 1207 (2020).